High-Resolution Vibrational Spectroscopy of *trans*-Formic Acid in Solid Parahydrogen

Leif O. Paulson and David T. Anderson*

Department of Chemistry, University of Wyoming, Laramie, Wyoming, 82071

Received: November 13, 2008; Revised Manuscript Received: January 7, 2009

We report high-resolution vibrational spectra of six normal modes of *trans*-formic acid (FA) in rapid vapor deposited solid parahydrogen (pH_2) with particular emphasis on the carbonyl stretching mode (ν_3) at ~1770 cm^{-1}. Infrared spectra in the ν_3 and $2\nu_3$ regions reveal that even in 99.99% enriched pH_2 samples, residual orthohydrogen (oH_2) present in the solid preferentially clusters to FA producing measurable shifts in the ν_3 transition frequency. The individual $FA(oH_2)_n$ cluster peaks in the size range from $n = 0$ to $n = 5$ are resolved, permitting unambiguous assignment of the ν_3 and $2\nu_3$ transition frequencies and linewidths for FA with a first solvation shell ($n = 0$) of only pH_2 molecules. This $n = 0$ feature is well fit by a Lorentzian line shape with a line width of 0.214(6) cm^{-1} and 0.45(2) cm^{-1} for ν_3 and $2\nu_3$, respectively, which is surprisingly broad for a small nonrotating molecule trapped in solid pH_2. Implications of the broad FA ν_3 Lorentzian line shape in terms of homogeneous and inhomogeneous broadening mechanisms are discussed.

1. Introduction

There is continued growth in the number and types of matrix isolation studies that utilize molecular hydrogen (H_2) as the host matrix.[1−21] Cryogenic molecular hydrogen crystals are unique host materials for both the low temperature spectroscopy and chemistry of embedded chemical dopants for three basic reasons. First, solid molecular hydrogen (SMH) is a quantum crystal which means that the zero-point translational motion of each H_2 molecule around its equilibrium position in the crystal lattice is a significant fraction (e.g., 18%) of the nearest-neighbor spacing within the crystal.[22] This large amplitude zero-point motion inflates the lattice spacing of the crystal and helps to remove defects resulting in a minimally perturbing homogeneous matrix host for high-resolution spectroscopy of embedded molecules. Second, the gas-phase vibrational and rotational quantum numbers of the H_2 molecule are conserved in the solid due to the weak H_2-H_2 intermolecular forces.[23] This permits detailed spectroscopic studies of the hydrogen host itself where the quantum labels of the initial and final states can be clearly specified. Third, at the temperatures where SMH is stable, nuclear spin restrictions on the H_2 wave function result in the parahydrogen (pH_2) molecules populating exclusively $J = 0$ rotational states and orthohydrogen (oH_2) molecules occupying $J = 1$ states. Since nuclear spin conversion in the absence of a paramagnetic catalyst is very slow in the solid,[22] nonequilibrium distributions of oH_2 and pH_2 can be generated in SMH to study how these two forms of H_2 interact differently with trapped dopant species. The different interactions arise due to rotational averaging of the H_2 angular coordinates over the H_2-dopant intermolecular potential, which for oH_2 results in both isotropic and anisotropic intermolecular interactions, but for pH_2 in a $J = 0$ state the anisotropic interactions average to zero.

This third feature of SMH deserves further discussion since the literature contains reports by researchers who use normal hydrogen (nH_2), a 25%:75% mixture of pH_2 and oH_2, as a matrix host while others like us use nearly pure pH_2 matrices. Under the low temperature conditions where SMH is stable, the different physical behaviors of oH_2 and pH_2 are most pronounced. In cryogenic SMH, the $J = 1$ oH_2 molecules possess an electric quadrupole moment that survives rotational averaging while for pH_2 in a $J = 0$ state the quadrupole moment rigorously averages to zero. Accordingly, the $J = 1$ oH_2 species have electrostatic interactions (e.g., dipole−quadrupole) with polar dopant species that are absent for the pH_2 molecules. This has two important ramifications for the high resolution spectroscopy of embedded molecules in these two types of hydrogen matrices: (1) in general matrix isolation studies in nH_2 will produce measurably different matrix shifts than analogous studies in enriched pH_2 crystals and (2) even in highly enriched pH_2 crystals the greater long-range attractive forces between polar dopant species and residual oH_2 can lead to preferential solvation of the dopant by oH_2. Both of these two points will be illustrated in the present study.

In this work we chose to study the infrared (IR) spectroscopy of formic acid (FA, HCOOH) in highly enriched (99.99%) solid pH_2 matrices as a means of investigating the high resolution vibrational spectrum of FA. The idea is to quench the rotational motion of FA by trapping it in solid pH_2 and then utilize the weakly perturbing nature of the pH_2 host to measure the frequencies, intensities, and detailed lineshapes of the various normal modes of FA. The FA molecule was chosen as a test case because the IR spectrum of FA has been recorded in a variety of cryogenic media such as solid neon[24] and argon,[25,26] solid nH_2,[27] and liquid helium nanodroplets.[28] FA is the simplest carboxylic acid, has only nine vibrational modes, and can exist in two planar structures, the *cis* and *trans* conformers with 0° and 180° H−C−O−H dihedral angles, respectively, where interconversion corresponds to rotation of the OH group around the CO bond. At room temperature, the *trans* conformer is favored by about 830:1 compared to the *cis* isomer, and thus in these low temperature studies only the *trans* isomer is important.[29] Another reason for choosing to study FA is provided by the recent studies from the Räsänen group which show that vibrational excitation of the nH_2 matrix host leads to *trans* → *cis* isomerization of the embedded FA dopant species,[27] which is an intriguing energy transfer process and thus high-resolution spectroscopic studies of FA isolated in solid pH_2 should prove useful.

---

* Electronic address: danderso@uwyo.edu.

10.1021/jp8100255 CCC: $40.75 © 2009 American Chemical Society
Published on Web 02/11/2009

The rest of this paper is organized as follows: section 2 describes computational efforts to calculate the vibrationally averaged dipole moment of FA in the $v_3 = 0$, 1, and 2 vibrational states which are used later to estimate vibrational shifts in the FA ν_3 vibrational transition frequency caused by replacing a single pH_2 by an oH_2 molecule in the first solvation shell of FA. Section 3 presents the experimental apparatus and details required to synthesize FA doped pH_2 solids with variable concentrations of oH_2. In section 4, we report the spectroscopic results and analysis used to identify oH_2 clustering to FA as the dominant broadening mechanism for high-resolution vibrational spectroscopy of FA in pH_2 matrices, assign spectra in the ν_3 and $2\nu_3$ regions to individual $FA(oH_2)_n$ clusters, and discuss the $n = 0$ cluster feature's line shape in terms of both homogeneous and inhomogeneous broadening mechanisms. In section 5, we summarize our conclusions on the high-resolution vibrational spectroscopy of FA in solid pH_2.

2. Electrostatic Modeling of oH_2-Induced ν_3 Vibrational Shifts

We can qualitatively predict, via a simple model, the shift in the ν_3 transition frequency of FA upon complexation with a single oH_2 molecule in solid pH_2 using electrostatic model calculations.[30] The oH_2-induced shift in the ν_3 transition of FA completely solvated by pH_2 molecules ($n = 0$) and with one nearest neighbor oH_2 molecule ($n = 1$) reflects the difference in the intermolecular interactions of FA with pH_2 and oH_2. In the following discussion, the n term specifies the number of oH_2 molecules in the first solvation shell of the FA molecule. The major difference between the interaction of FA with pH_2 or oH_2 is that the oH_2 molecule has a quadrupole moment that survives rotational averaging over the $J = 1$ wave function while for pH_2 in a $J = 0$ state, the quadrupole moment averages to zero. Thus, while induction and dispersion interactions are operative for both pH_2 and oH_2, electrostatic interactions are only possible for oH_2. This allows the $n = 0$ to $n = 1$ vibrational shift to be approximated by the change in the electrostatic interaction of the isolated FA-oH_2 cluster upon vibrational excitation of the FA. The distance (and conformation) between the FA and oH_2 molecules and the values for the dipole moment of FA in the ground and vibrationally excited states are required for this calculation.

The electrostatic interaction between FA and oH_2 is modeled using the dipole−quadrupole interaction,[31] namely

$$V_{dq}(R, \theta_1, \theta_2, \varphi) = \frac{3\mu_1\Theta_2}{2R^4}[\cos\theta_1(3\cos^2\theta_2 - 1) + 2\sin\theta_1\sin\theta_2\cos\theta_2\cos\varphi] \quad (1)$$

where FA is defined as molecule 1 and H_2 is molecule 2, as designated by the subscripts, and μ and Θ are the dipole and quadrupole moments, respectively. By assumption that the FA and oH_2 molecules adopt the minimum energy dipole−quadrupole configuration (i.e., linear configuration with $\theta_1 = 0$, $\theta_2 = 0$, and $\phi = 0$) and that $R = 3.79$ Å, the nearest neighbor spacing in a pH_2 crystal, the only values required to calculate the dipole−quadrupole interaction are the quadrupole moment of oH_2 and the vibrationally averaged dipole moments of FA. The quadrupole moment of oH_2 is set to the effective value for oH_2 at cryogenic temperatures, $\Theta_2 = ((2)/(5))\Theta_{v=0,J=1} = 0.19441$ au.[22] Although the ground and first ν_3 excited-state dipole moments of FA have been measured using Stark spectroscopy,[32] to the best of our knowledge the value for the second excited-state has not been published. Therefore, for consistency, we computed dipole moments for the $v_3 = 0$, 1, and 2 vibrational states of FA to use in these electrostatic model computations. The procedure for the calculation of these dipole moments is briefly summarized below where the details will be the subject of a separate publication.

TABLE 1: Calculated and Experimental FA Dipole Moments for Selected ν_3 Vibrational States in Units of Debye (D)[a]

v_3	μ_{calc}	μ_{expt}[b]	V_{dq}	Δ_{calc}	Δ_{expt}
0	1.4231	1.4253	27.28		
1	1.4645	1.4512	28.07	−0.79	−0.32
2	1.5055		28.86	−1.58	−0.65

[a] The calculated dipole−quadrupole potential (V_{dq}) interaction using eq 1 and the calculated (Δ_{calc}) and measured (Δ_{expt}) vibrational shifts, all in units of cm^{-1}. [b] Reference 32.

A quantum mechanical package (Gaussian 98)[33] was used to calculate the harmonic vibrational frequencies and normal modes of FA. By use of the normal mode displacement vectors for the ν_3 mode, a series of 40 structures were generated at discrete steps along the ν_3 normal mode coordinate ranging from −0.35 to 1.0 Å. The energy profile and dipole moment along the normal mode displacement were then computed for these 40 structures at the same level of theory as the vibrational frequencies and normal modes. Next, the Schrödinger equation was solved numerically for the resulting energy profile using the grid variational method[34] to get the vibrational wave functions. These calculations were performed using MATLAB (Mathworks Inc. Mattick, MA). Finally, the vibrationally averaged dipole moments were obtained from,

$$\mu_n = \int \psi_n(q)\mu(q)\psi_n(q)_{dq} \quad (2)$$

where ψ_n is the wave function of the nth vibrational state and μ is the dipole moment as a function of normal mode displacement (q). Equation 2 was integrated numerically, and several levels of theory and basis sets were tested. The calculated results that were most consistent with the experimental gas-phase frequencies[35] and measured dipole moments[32] were obtained at the DFT: BPW91/cc-pVDZ level. The calculated dipole moments for the $v_3 = 0$, 1, and 2 states are compared with values measured using Stark spectroscopy[32] in Table 1. The agreement between the calculated and experimental dipole moments is very good (<1%). Therefore, these theoretical values of the vibrationally averaged dipole moments are used in the electrostatic model calculations using eq. 1. In section 4D, the results of the calculated shifts will be presented and discussed.

3. Experimental Section

The experimental apparatus designed to synthesize and characterize chemically doped pH_2 solids is based on the "rapid vapor deposition" methodology of Fajardo and co-workers[36,37] and has been described in detail elsewhere.[30,38] Briefly, doped solid pH_2 samples are prepared by the codeposition of independent gas flows of dopant (e.g., FA) and precooled pH_2 onto a BaF_2 optical substrate cooled to ~2.5 K in a sample-in-vacuum liquid helium bath cryostat (Janis SSVT-100). Room temperature nH_2 gas is precooled and enriched in the para nuclear spin state during deposition using a home-built ortho/para (o/p) converter. The o/p converter consists of a $^1/_8$-in. outer diameter by 2 m long copper tube packed with 4.5 g of $Fe(OH)_3$ catalyst particles ranging in size from 10−100 μm, wound and potted with thermal conducting epoxy onto an oxygen-free high conductivity copper bobbin that can be cooled to a minimum temperature of

10 K by a closed-cycle helium cryostat (Advanced Research Systems CSW-204). In these studies, the o/p converter was purposely maintained at temperatures of 14, 20, and 25 K to produce, respectively, pH_2 crystals with 45, 1800, and 9600 ppm concentrations of oH_2. These oH_2 concentrations are calculated using the rotational partition function of H_2 and assume full thermal equilibration of the nuclear spin states at the stated o/p converter temperature. The actual oH_2 concentration can be checked via infrared absorption measurements of the ortho-induced $Q_1(0)$ feature at 4153 cm^{-1}, and these measurements show that the actual concentrations are all within +50% of the calculated values.[39] For simplicity therefore, the calculated oH_2 concentrations will be used throughout the paper. Operating the o/p converter at temperatures below 14 K results in “plugging” of the converter; this is presumably due to freezing of the two-phase H_2 gas/liquid mixture in the converter which severely limits flow. Therefore, 14 K is the lowest o/p converter temperature that can be utilized with this apparatus to generate the most highly enriched pH_2 solids. The path length or sample thickness was determined using the empirical correlation developed by Tam and Fajardo between the integrated intensity of the $Q_1(0) + S_0(0)$ or $S_1(0) + S_0(0)$ pH_2 infrared “double” transitions and sample thickness.[40]

For these experiments, the flow rate of nH_2 gas was between 150−210 mmol h^{-1}, enabling 2.7(2) mm thick samples to be grown in less than one hour. Reagent grade formic acid (Sigma-Aldrich ACS Reagent 88%) was subjected to repeated freeze−pump−thaw cycles prior to use to remove volatile impurities. The room temperature vapor pressure from liquid FA was used to make low pressure FA gas samples in the dopant manifold. The flow rate of FA was adjusted to achieve approximately 2 to 20 ppm FA concentrations in solid pH_2.

The infrared absorption spectra of FA doped pH_2 solids are obtained with a Fourier transform infrared (FTIR) spectrometer at a resolution of 0.02 cm^{-1} (nominal with boxcar apodization). Peak widths discussed herein refer to decadic absorbance measurements. No attempt was made to deconvolute the spectra. The FTIR spectrometer (Bruker IFS 120 HR) is equipped with a globar source, a Ge-coated KBr beamsplitter, and a liquid nitrogen cooled HgCdTe detector for these experiments. The entire optical path outside of the spectrometer and cryostat vacuum shroud is purged with dry N_2 gas to reduce atmospheric absorptions. The samples are annealed by raising the temperature of the solid to 4.3 K for a specified period of time. As-deposited spectra are recorded immediately after deposition and have never been exposed to temperatures above 2.5 K. The temperature range between 1.7 and 4.3 K is achieved by vacuum pumping on the helium bath cryostat.

4. Results and Discussion

We present the IR spectra for six of the nine normal modes of FA isolated in solid pH_2 matrices. The measured peak frequencies are compared to literature values for FA in the gas-phase and isolated in solid Ne, Ar, and nH_2 matrices. From this comparison, it is clear that nH_2 matrices produce slightly greater matrix shifts in the FA vibrational frequencies than pH_2 matrices due to the large oH_2 content in solid nH_2. High resolution measurements reveal that all the FA vibrational transitions are inhomogeneously broadened in pH_2 matrices. Detailed measurements of the most intense FA vibrational mode, the ν_3 carbonyl stretch, as a function of the oH_2 concentration in the crystal, indicate that oH_2 clustering to FA is responsible for the line broadening observed for FA isolated in highly enriched pH_2 matrices. Multiple relatively sharp (~0.2 cm^{-1}) peaks are spectrally resolved in the ν_3 region and assigned to $FA(oH_2)_n$ clusters ranging in size from $n = 0$ to $n = 5$, where n denotes the number of oH_2 molecules in the cluster. The $FA(oH_2)_n$ clusters are also investigated in the $2\nu_3$ region permitting the ν_3 anharmonicity constant for FA isolated in solid pH_2 to be determined. Assignment of the multiple peak ν_3 spectra to oH_2 clustering is confirmed by observing intracluster oH_2 to pH_2 nuclear spin conversion and by comparison of the measured oH_2-induced ν_3 vibrational shifts with electrostatic model calculations using calculated dipole moments for FA in the ν_3 = 0,1, and 2 vibrational states. Finally, the ν_3 and $2\nu_3$ $FA(oH_2)_n$ cluster spectra are fit to a sum of Lorentzian lineshapes to extract the width of the $n = 0$ feature. If the measured line width of the ν_3 fundamental corresponds to homogeneous broadening, then the lifetime of the initial vibrational excitation is 25 ps, which is extremely short for a five-atom molecule trapped at low concentration in a pH_2 host.

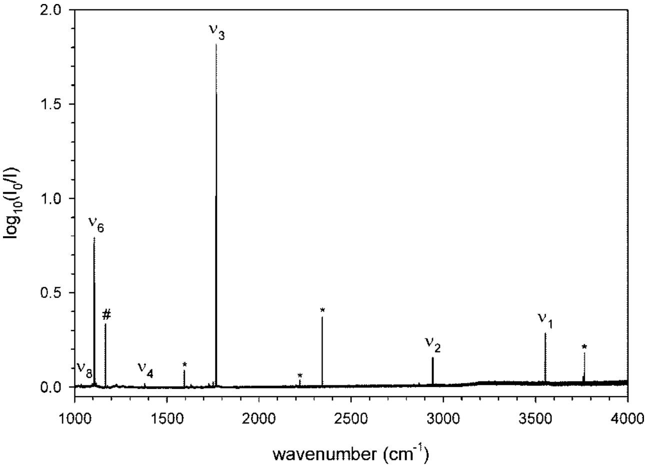

Figure 1. Survey spectrum of FA doped pH_2 recorded at 1.68 K with a resolution of 0.02 cm^{-1} after annealing with an oH_2 concentration of 70 ppm. FA absorptions labeled by normal mode assignment (see text for details).

A. FA Vibrational Frequencies in pH_2 Matrices. A survey spectrum of FA isolated in solid pH_2 is shown in Figure 1 which contains absorption features for six of the nine normal modes of FA. All of the FA peaks in Figure 1 are labeled with the corresponding normal mode assignment. The peak marked with the number sign denotes the $U_0(0)$ solid hydrogen absorption.[11] The peaks marked with an asterisk denote either H_2O, CO_2, or N_2O impurity absorptions.[11,41,42] The FA peak assignments, frequencies, and matrix shifts ($\Delta\nu_{matrix} = \nu_{para} - \nu_{gas}$) for FA isolated in solid pH_2 are listed in Table 2 including the literature values for FA in Ne, Ar, and nH_2 matrices as well as the gas-phase values.[24,25,27,35] First, note that the FA transition frequencies are comparable in nH_2 and pH_2 matrices. In both matrices the ν_1 and ν_3 modes show red shifts while the ν_2, ν_4, ν_6, and ν_8 normal modes display blue shifts. However, upon closer scrutiny the matrix shifts for pH_2 and nH_2 differ systematically, with the pH_2 values always closer to the gas-phase transition frequencies for both red and blue matrix shifts. As discussed in the introduction, the larger matrix shifts for nH_2 compared to pH_2 likely arise from the greater long-range electrostatic interactions of FA with oH_2, that is, the intermolecular forces of FA with oH_2 are greater than with pH_2 and thus cause larger magnitude matrix shifts. While generalization of the matrix shifts measured for FA in nH_2 and pH_2 matrices to other dopant species is premature due to the limited set of observations, it is clear that the two distinct forms of molecular hydrogen namely oH_2 and pH_2 result in slightly different matrix shifts for nH_2

TABLE 2: Vibrational Frequencies and in Parentheses the Matrix Shift ($\Delta\nu_{matrix}$) of FA Isolated in Ar, Ne, nH_2, and pH_2 Matrices[a]

mode	Ar[b]	Ne[c]	nH_2[d]	pH_2	gas[e]
a′ ν_1 ν(OH)	3550.4 (−20.1)	3569.4 (−1.1)	3551 (−19.5)	3553.69 (−16.81)	3570.5
a′ ν_2 ν(CH)	2952.9 (+10.8)	2937.8 (−4.3)	2946 (+3.9)	2942.07 (+0.01)	2942.06
a′ ν_3 ν(C=O)	1767.2 (−9.6)	1773.9 (−2.9)	1765.5 (−11.3)	1768.63 (−8.20)	1776.83
a′ ν_4 ν(C−O)	1381.0 (+1.0)	1379.7 (−0.3)	1383 (+3.0)	1380.62 (+0.62)	1380
a′ ν_5 δ(CH)	1215.8 (−7.2)	1217.6 (−5.4)	1218 (−5.0)	[f]	1223
a′ ν_6 δ(OH)	1103.4 (−1.5)	1102.8 (−2.1)	1109 (+4.1)	1106.69 (+1.84)	1104.85
a″ ν_8 δ(CH)	1037.4 (+3.9)	1035.6 (+2.1)	1037 (+3.5)	1035.33 (+1.86)	1033.47

[a] Gas-phase values are included for comparison. All values in units of cm^{-1}. [b] Reference 25. [c] Reference 24. [d] Referemce 27. [e] Referemce 35. [f] Only broad peaks are observed in this region.

and pH_2 matrices, and this should be taken into account when comparing results.

The a priori prediction of matrix shifts for a given dopant species in different matrix isolation hosts is difficult due to the delicate balance between repulsive and attractive guest−host interactions in matrices composed of different host materials and with different cavity sizes for dopant molecules. Jacox compiled an extensive array of data for species deposited in a variety of cryogenic matrices.[43,44] In one of these papers Jacox reports,[43] "Matrix shifts are smallest for neon, increase with increasing atomic mass of the rare gas, and are largest for nitrogen." The matrix shifts in Ne matrices are usually within 1% of the gas-phase value and for Ar matrices, most of the diatomic molecules are usually less than 2%.[43] Thus it is interesting to compare the results for pH_2 with those of Ne and Ar matrices.

The matrix shifts observed for FA in a Ne matrix are consistently small (<0.5%) owing to the very weak Ne solvation effect. The dopant-Ne interactions are dominated by induction and dispersion which for Ne with a small polarizability are both very weak. The matrix shifts observed for FA in pH_2 and Ne matrices are of similar magnitudes except for the ν_1 and ν_3 stretching modes, where pH_2 produces significantly larger matrix shifts than Ne (see Table 2). The comparable matrix shifts in Ne and pH_2 is the result of a balance between two properties of the solids. The polarizability of Ne ($\alpha = 0.3956$ Å^3) is less than pH_2 (0.8023 Å^3), and therefore Ne matrices should be less perturbing.[45] The greater mass, however, of Ne compared to pH_2 means that at cryogenic temperatures the pH_2 molecules in the crystal have substantially greater translational zero-point motion. This increased zero-point motion results in an expansion of the nearest neighbor spacing such that the 3.78 Å lattice spacing in solid pH_2 is significantly greater than the 3.16 Å value in solid Ne.[46] The greater zero-point motion in the pH_2 crystals should keep the first solvation shell of pH_2 molecules further away from the dopant species thus producing smaller matrix shifts compared to Ne. These two competing effects, polarizability and zero-point motion, allow for Ne and pH_2 matrices to have reasonably small matrix shifts.

The Ar matrix results in the literature show greater matrix shifts for FA than either the Ne or pH_2 matrix data, consistent with the survey results of Jacox.[43,44] For comparison,[45,47] the nearest-neighbor spacing in Ar at 4 K is 3.755 Å and Ar has a polarizability of 1.6411 Å^3. The cavity size in Ar is comparable to pH_2, and yet Ar has a polarizability about twice that of pH_2. Thus, it is interesting that the two stretching vibrations that show much larger matrix shifts to lower energy in pH_2 compared to Ne similarly show large matrix shifts to lower energy in Ar. This seems to suggest that, for the ν_1 and ν_3 stretching modes, the matrix shift in Ne contains significant contributions from repulsive interactions which are more or less absent for both Ar and pH_2 matrices. Thus, it seems pH_2 behaves somewhere between Ne and Ar matrices with most bending fundamentals displaying matrix shifts similar to Ne but the two stretching fundamentals (ν_1 and ν_3) more like Ar. Note that the ν_2 stretch displays a large positive matrix shift in Ar but only a negligible blue shift in solid pH_2.

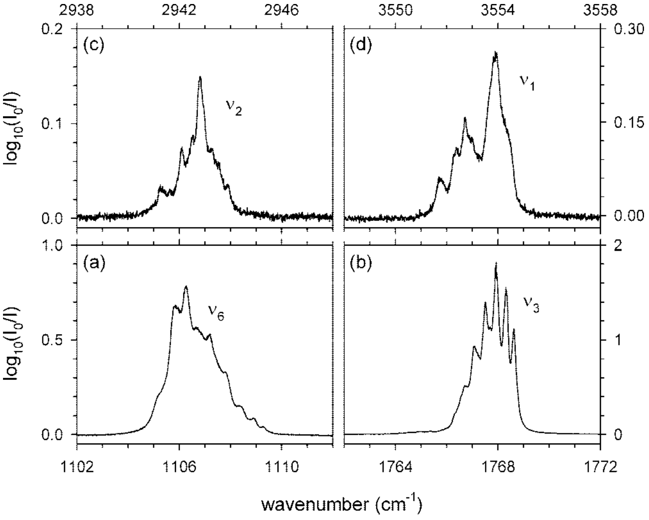

Figure 2. Enlargement of the spectrum shown in Figure 1 in the region of the (a) ν_6, (b) ν_3, (c) ν_2, and (d) ν_1 vibrational modes.

B. oH_2 Clustering to FA in pH_2 Matrices. An inhomogeneous broadening mechanism present in pH_2 matrices that is not important in rare gas matrices is due to the presence of residual oH_2 species in enriched pH_2 solids. The FA absorptions in Figure 1 appear sharp and symmetric, but upon closer inspection, each FA absorption feature shows evidence of broadening and fine structure. The spectra in Figure 2 show expanded views of the ν_6, ν_3, ν_2, and ν_1 absorptions of FA. The broadening and fine structure shown in Figure 2 is due, at least in part, to clustering of oH_2 molecules to the FA dopant as will be shown. As demonstrated previously for small polar dopant molecules (H_2O, CH_3F, and N_2O), even trace amounts of oH_2 present in highly enriched pH_2 crystals can preferentially cluster to the dopant species being studied and induce small but measurable shifts in the dopant vibrational frequencies and in some cases creating new cluster absorption features.[11,38,42] The oH_2 molecules are attracted to the polar dopant species due to the nonzero oH_2 quadrupole moment. This dipole−quadrupole interaction provides a small thermodynamic driving force for oH_2 to replace pH_2 in the first solvation shell around the dopant; however, even small energetic differences can become insurmountable at liquid helium temperatures and thus oH_2 cluster formation is usually irreversible. For rapid vapor deposited samples upon the first annealing cycle, it is generally found that the amount of oH_2 clustering to the dopant increases.[30,38]

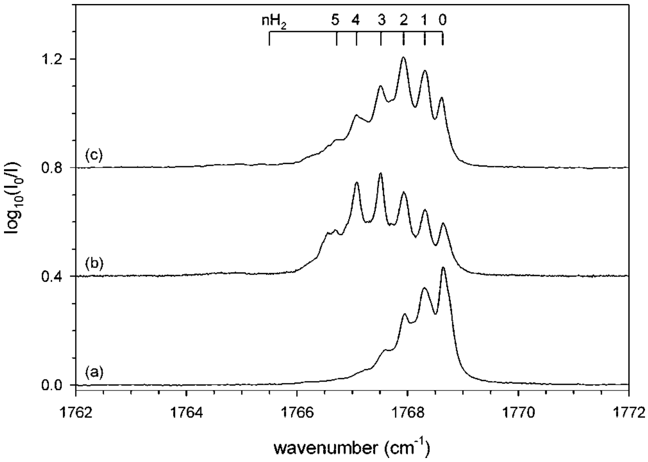

Figure 3. IR spectra of FA-doped pH_2 detailing the effects of annealing on the ν_3 absorption feature for a 45 ppm oH_2 concentration sample. Trace a is recorded at 1.80 K immediately after deposition; trace b is recorded while annealing the sample at 4.33 K; trace c is recorded after lowering the temperature to 1.62 K. The $FA(oH_2)_n$ cluster frequencies are shown on the scale at the top, labeled by *n,* the number of oH_2 molecules.

All four of the FA vibrational modes presented in Figure 2 show evidence of oH_2 clustering: namely, the observed peak maxima and lineshapes depend on the oH_2 concentration in the sample and show pronounced irreversible changes upon annealing the as-deposited sample.

Of the four absorptions shown in Figure 2, the ν_3 absorption at ~1768 cm^{-1} shows the simplest and best resolved structure, making it the most promising vibrational mode for detailed analysis. The multiple peak structure in the ν_3 spectrum is a form of spectral inhomogeneity caused by discrete differences in the number of nearest neighbor oH_2 molecules clustered to the FA dopant. Each peak in the ν_3 spectrum is uniquely assigned to a specific $FA(oH_2)_n$ cluster, which form in the pH_2 solid during deposition and upon annealing the as-deposited sample. In the case of the other three fundamental absorptions in Figure 2, inhomogeneities in the absorptions due to oH_2 clustering must also be present, but individual $FA(oH_2)_n$ cluster features are not resolved, and thus a unique cluster assignment for these absorptions is not possible. Therefore, in this work, we will focus on using the ν_3 vibrational mode of FA to probe the phenomenon of oH_2 clustering in order to determine the ν_3 line shape in the limit of pure pH_2 crystals. The ν_3 absorption can also be used to quantitatively illustrate how the absorption feature changes as a function of the oH_2 concentration in the sample.

C. $FA(oH_2)_n$ Clusters Observed via ν_3 and $2\nu_3$. Figure 3 demonstrates the irreversible growth in $FA(oH_2)_n$ cluster size upon annealing the sample. Trace a in Figure 3 was recorded at 1.80 K for an as-deposited sample with an oH_2 concentration of 45 ppm, the minimum oH_2 concentration that can be achieved. Each peak is assigned to a specific $FA(oH_2)_n$ cluster size where the *n* assignment is indicated by the scale at the top of the figure and the cluster peak frequencies are presented in Table 3. The peak with the greatest transition frequency (1768.63 cm^{-1}) is assigned as the $n = 0$ peak, i.e., the limit where FA is solvated by only pH_2 molecules in the first solvation shell. The frequency labeled nH_2 is the value measured by Marushkevich et al.[27] for FA solvated in nH_2 and therefore approximates the other limit where FA is solvated nearly completely by oH_2 molecules. Each oH_2 molecule that clusters to FA shifts the ν_3 transition frequency to lower energy. The shift caused by the first 5 oH_2 molecules is found to be nearly constant; however, the approach to the nH_2 limit is highly nonlinear. The first ~5 oH_2 molecules cluster to the FA in nearly equivalent solvation shell sites causing a nearly constant shift per oH_2 molecule in the FA ν_3 frequency. The dominant interaction responsible for perturbing the ν_3 vibrational mode upon oH_2 clustering is an electrostatic dipole–quadrupole interaction which falls off as R^{-4}. Thus, the oH_2 molecules that occupy first solvation shell sites and are in close proximity to the FA dopant produce the greatest shifts, while subsequent oH_2 molecules that occupy solvation sites further removed from the FA molecule cause incrementally smaller shifts. In the case of FA, the cluster peaks $n = 0-5$ are resolved, but the peaks of the larger clusters overlap.

TABLE 3: Measured ν_3 and $2\nu_3$ Vibrational Frequencies and Incremental Shifts ($\Delta\nu$) for $FA(oH_2)_n$ Clusters Isolated in Solid pH_2 (All Values in cm^{-1})

n	ν_3	$\Delta\nu$	$2\nu_3$	$\Delta\nu$
0	1768.63		3518.42	
1	1768.31	−0.32	3517.77	−0.65
2	1767.93	−0.38	3517.07	−0.70
3	1767.51	−0.42	3516.21	−0.86
4	1767.08	−0.43		
5	1766.72	−0.36		

Trace b in Figure 3, the annealing scan, is recorded the first time the temperature of the sample is increased to 4.33 K after deposition. Cluster growth occurs very rapidly after the temperature is raised to 4.33 K. As shown in Figure 3, annealing the sample causes the cluster distribution to shift toward larger cluster sizes. In the scan of the as-deposited sample, the cluster peak with maximum intensity is the $n = 0$ feature while in the annealing spectrum the dominant cluster size shifts to $n = 3$. Upon annealing, oH_2 molecules within some critical distance from the FA dopant species are attracted to the dopant and displace the pH_2 molecules in the first solvation shell around the FA dopant causing the intensity of the larger $FA(oH_2)_n$ cluster peaks to increase. This cluster growth is most dramatic the first time the as-deposited sample is annealed. After the annealing spectrum is recorded, the temperature of the sample is reduced to 1.62 K and the low temperature annealed spectrum is recorded which is shown in trace c of Figure 3. Comparison of traces b and c in Figure 3 shows that the cluster distribution shifts back slightly toward smaller cluster sizes in the low temperature annealed sample. As will be discussed later, this shift toward smaller cluster sizes is not due to lowering the temperature but rather reflects intracluster oH_2 to pH_2 nuclear spin conversion.

A similar series of spectra are shown in Figure 4 for a FA doped solid pH_2 crystal with a greater oH_2 concentration. Trace a in Figure 4 was recorded at 1.81 K for an as-deposited sample with an oH_2 concentration of 9600 ppm. Individual cluster sizes are just resolved in the as-deposited sample with cluster sizes in the range $n = 2-5$ showing maximum intensity. In comparison to the as-deposited spectra in Figure 3 for the 45 ppm oH_2 sample, the 9600 ppm oH_2 sample in Figure 4 shows that FA is solvated by greater numbers of oH_2 molecules as expected. In addition, the greater oH_2 concentration broadens the individual cluster features. Trace b in Figure 4 was recorded at 4.31 K while annealing the sample. Upon annealing, the cluster distribution shifts toward larger cluster sizes as evidenced by the collapse of the multiple peak cluster spectra into a single feature at lower wavenumber. The individual cluster sizes are no longer resolved in this cluster size range and thus only a single, broad asymmetric ν_3 peak is observed. Note that, even in this 9600 ppm oH_2 sample (1% oH_2), the transition wave-

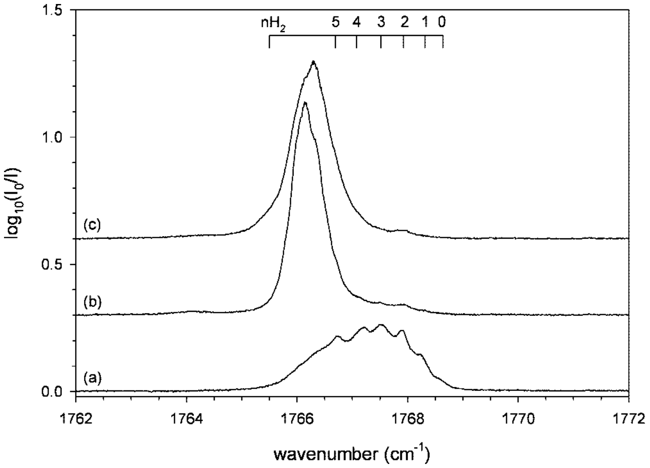

Figure 4. A similar series of spectra as shown in Figure 3 for a FA-doped pH_2 sample with 9600 ppm oH_2. Trace a is recorded at 1.81 K immediately after deposition; trace b is recorded while annealing the sample at 4.31 K; trace c was recorded after lowering the temperature to 1.63 K. The $FA(oH_2)_n$ cluster frequencies are shown on the scale at the top, labeled by n, the number of oH_2 molecules.

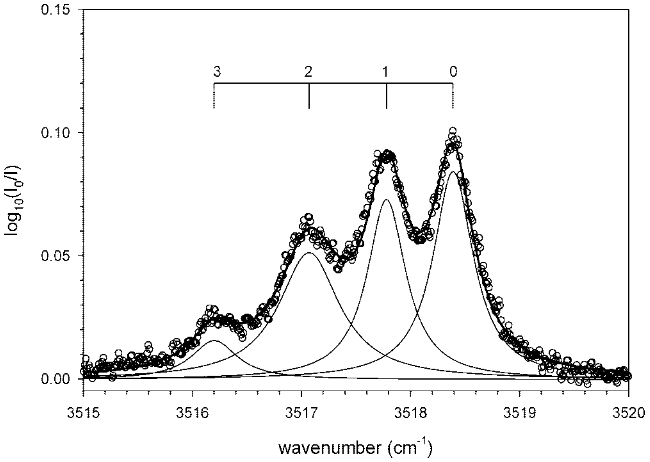

Figure 5. The circles represent the IR data, the heavy line denotes a least-squares fit to a sum of four Lorentzian lineshapes, and the thin lines are the individual fitted peaks.

number of the observed ν_3 feature is more than $^3/_4$ of the way from the $n = 0$ peak to the full nH_2 limit. The incremental shift in the ν_3 absorption feature with added solvating oH_2 molecules is greatest for the first ~5 oH_2 molecules and then falls off with an R^{-4} distance dependence since the shift is primarily due to dipole−quadrupole electrostatic interactions. Thus, since the incremental shift decreases with increasing cluster size, even at 1% oH_2 concentrations the peak maximum is observed to be 75% of the limiting value observed in nH_2 matrices. In addition, at 1% oH_2 concentrations the FA molecules are solvated in relatively large $FA(oH_2)_n$ clusters so the ν_3 absorption feature is more homogeneous, the n and $n+1$ inhomogeneities in this cluster size range are very small and not resolved.

The $FA(oH_2)_n$ cluster spectrum should have a similar spectral signature in the $2\nu_3$ spectral region. Figure 5 shows the $2\nu_3$ spectrum recorded at 1.79 K for an annealed FA doped pH_2 solid with a 45 ppm oH_2 concentration. To observe this weaker FA overtone transition, the FA concentration was deliberately increased to ~20 ppm. In Figure 5 the spectral data are represented as circles and the line represents a least-squares fit of the data to a sum of four Lorentzian lineshapes (more discussion in section 4F). Consistent with the ν_3 fundamental studies, multiple peaks are observed in the overtone region with the peaks to lower frequency increasing in intensity upon annealing. Accordingly, the peaks in the overtone region are assigned to $FA(oH_2)_n$ clusters, with the peak at the greatest transition energy (3518.42 cm^{-1}) assigned to the $n = 0$ cluster. The measured cluster peak frequencies for $2\nu_3$ are presented in Table 3 and indicated by the scale at the top of Figure 5.

By use of the $n = 0$ frequencies for FA in the ν_3 and $2\nu_3$ spectral regions, the harmonic frequency (ω_e) and anharmonicity constant ($\omega_e x_e$) for the ν_3 mode of FA isolated in solid pH_2 are calculated to be $\omega_e = 1787.47(5)$ cm^{-1} and $\omega_e x_e = 9.42(2)$ cm^{-1}, respectively, where the errors in parenthesis reflect propagation of errors based on the uncertainties in the $n = 0$ transition frequencies. These values are very similar to effective constants ($\omega_3^0 = 1786.1$ cm^{-1} and $x_{33} = 9.3$ cm^{-1}) extracted from more extensive fits to gas-phase data suggesting the perturbations of the pH_2 matrix on the vibrational constants of FA are minimal.[35]

D. Computation of oH_2-Induced ν_3 Vibrational Shifts. In support of our arguments concerning the assignment of the ν_3 multiple peak structure to oH_2 clustering, we have used a simple model to calculate oH_2-induced ν_3 vibrational shifts. In section 2 we presented the calculation of vibrationally averaged dipole moments of the ν_3 mode of FA. Those dipole moments, coupled with the effective quadrupole moment for a $J = 1$ oH_2 molecule and eq 1 allow the dipole−quadrupole potential (V_{dq}) to be calculated. This term V_{dq} represents the difference in solvation energy for the FA molecule by replacing one pH_2 molecule with an oH_2 molecule. On the basis of these model calculations $V_{dq} = 27.28$ cm^{-1} for the $\nu_3 = 0$ state of FA and thus the solvation energy of FA is lowered by approximately this amount upon complexation with a single oH_2 molecule. This simple model calculation does not take into account zero-point effects but an increase of tens of cm^{-1} also supports the experimental finding that solvation by oH_2 is irreversible at cryogenic temperatures (1.6−4.3 K). This "difference potential" approach has been used previously by Oka to study the shifts in the $Q_1(0)$ transition of D_2 and HD impurities in pH_2 matrices due to replacement of a nearest neighbor $J = 0$ pH_2 molecule by a $J = 1$ oH_2 molecule.[2] We also used this approach to interpret the ν_3 spectrum of CH_3F in highly enriched pH_2 solids.[30]

Returning to Table 1, we can approximate the measured $n = 0$ to $n = 1$ vibrational shifts (Δ_{expt}) for the ν_3 and $2\nu_3$ vibrational transitions using the calculated values of V_{dq} for the different vibrational states of FA. Given the approximations in Δ_{calc}, the level of agreement between Δ_{calc} and Δ_{expt} is highly satisfactory. The sign of the shift is correctly modeled and suggests that for the ν_3 mode the dominant intermolecular interaction between the oH_2 molecule and FA that contributes to the shift is caused by the dipole−quadrupole electrostatic interaction. Furthermore, the shift is greater for the $2\nu_3$ transition as expected by the increase in the FA vibrationally averaged dipole moment in the $\nu_3 = 2$ state. Even the approximate order of magnitude of the shift is reproduced for the ν_3 and $2\nu_3$ vibrational transitions by the simple electrostatic model calculations. A similar level of agreement was achieved for the ν_3 vibrational mode of CH_3F as reported previously.[30]

These simple model calculations will always predict oH_2-induced shifts to lower energy when the vibrationally averaged dipole moment of the dopant increases upon vibrational excitation. The ability to model the oH_2-induced shift by electrostatic arguments will not always be possible, and if significant changes in the vibrational averaged intermolecular potential occur due to other intermolecular forces such a model will not work. As displayed in Figure 2 only the ν_3 mode shows the simple progression in $FA(oH_2)_n$ cluster peaks to lower energy, and this

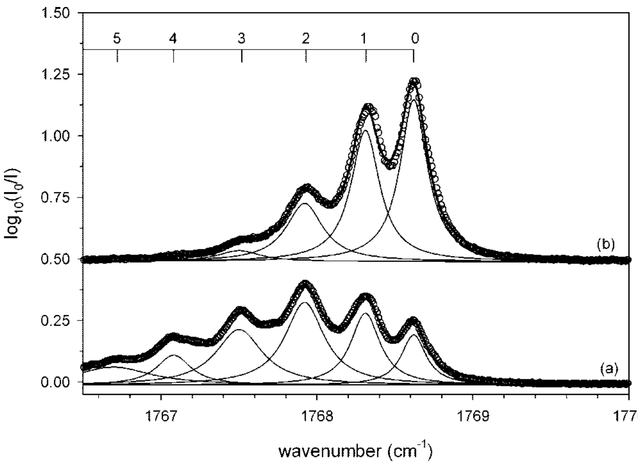

Figure 6. IR spectra in the ν_3 spectral region for FA doped pH_2 with an oH_2 concentration of 45 ppm that illustrates the effect of intracluster oH_2 to pH_2 nuclear spin conversion. Trace a is recorded at low temperature (1.57 K) right after annealing the sample at 4.33 K for approximately 1 h. Trace b is recorded 391 min after trace a while maintaining the sample at 1.57 K. The circles represent the IR data, the heavy line is the result of a least-squares fit to a sum of Lorentzian lineshapes, and the thin lines are the individual fitted peaks.

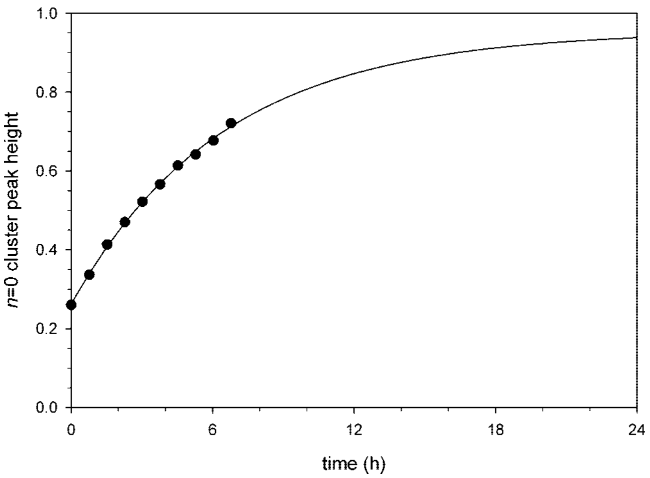

Figure 7. The filled circles are the ν_3 peak height data for the $n = 0$ cluster feature as a function of time for the sample shown in Figure 6. The solid line is the fitted exponential curve to eq 3.

is likely related to the fact that the ν_3 transition has the greatest oscillator strength[35] and thus represents the mode where the dipole moment of FA changes the most upon vibrational excitation making the oH_2-induced cluster shifts best modeled by electrostatic calculations.

E. $FA(oH_2)_n$ Intracluster oH_2 to pH_2 Nuclear Spin Conversion. Further evidence that the multiple peak structure in the ν_3 spectra of FA isolated in solid pH_2 is due to oH_2 clustering is provided by the experimental observation that the cluster distribution gradually shifts toward smaller cluster sizes with time, even when the sample is maintained at low temperature (e.g., 1.57 K). The process of intracluster oH_2 to pH_2 (o/p) nuclear spin conversion is illustrated in Figure 6. Trace a of Figure 6 shows the ν_3 spectrum of a FA-doped pH_2 sample recorded at low temperature right after annealing with an oH_2 concentration of 45 ppm. The experimental data in Figure 6 are indicated by circles, and the line through the data is the result of a least-squares fit to a line shape function generated from a sum of Lorentzian lineshapes. Trace b of Figure 6 is the spectrum of the same sample under identical conditions, except this spectrum was recorded 391 min after trace a. The total integrated absorbance of the two spectra in this region (1762−1772 cm^{-1}) is the same to within experimental uncertainty (±1%), but the intensity of the $n = 0$ and $n = 1$ peaks have increased at the expense of the $n \geq 2$ cluster peaks. Complete kinetic modeling of the intracluster o/p nuclear spin conversion process is beyond the scope of the present study. The focus is on the low oH_2 concentration limit for IR spectroscopy of FA in solid pH_2. To quantify the amount of time necessary to approach this pure pH_2 limit, the low oH_2 concentration data were analyzed. Specifically, the growth of the $n = 0$ peak with time is displayed in Figure 7 for the sample shown in Figure 6. The growth of the $n = 0$ feature is determined from the peak height of the $n = 0$ feature. The solid curve shown in Figure 7 is the result of a least-squares fit of the data to an equation of the form,

$$P(t) = A + B(1 - e^{-kt}) \qquad (3)$$

where $P(t)$ is the peak height and t is the time after the annealed sample is cooled to 1.57 K. The data shown in Figure 7 gave a rate constant of $k = 0.15(3)\ h^{-1}$ where the reported uncertainty is the 2σ value in the fitted rate constant. Previous work from this laboratory on $CH_3F(oH_2)_n$ cluster spectra revealed the growth of the $n = 0$ feature at 2.3 K with a rate constant $k = 0.25(6)\ h^{-1}$.[38] The similar magnitude of the two fitted rate constants suggests analogous processes are occurring for both $FA(oH_2)_n$ and $CH_3F(oH_2)_n$ clusters in solid pH_2. One difference however between CH_3F and FA is that CH_3F has nonzero total nuclear spin $I = {}^3/_2$ in the lowest $J = 0$, $K = 0$ rotational state due to the three equivalent hydrogens, while FA does not have any equivalent atoms. The magnitude of the dopant-induced nuclear spin conversion rate constants are significantly larger than the self-conversion rate typically reported 0.019 h^{-1}, which is second-order with respect to the oH_2 concentration and relies on two oH_2 molecules being nearest neighbors.[22] In these measurements we specifically measure the intracluster rate when the oH_2 molecule is bound to the FA molecule in a cluster. The increased rate constants measured in dopant clusters is consistent with NMR measurements at very low temperature which also find the self-conversion rate increases with decreasing oH_2 concentration due to the formation of oH_2 dimers.[22] Figure 7 also illustrates that based on these measurements it should take approximately 24 h for the ν_3 cluster spectra to develop into a single $n = 0$ absorption feature.

F. Formic Acid ν_3 Line Shape in Solid pH_2. Returning to Figure 6, recall that trace b was recorded at low temperature for a sample with an initial oH_2 concentration of 45 ppm more than 6 h after the sample was annealed, and thus due to intracluster o/p conversion this spectrum represents one of the lowest oH_2 concentrations studied. The $n = 0$ feature denotes FA completely solvated by pH_2 molecules in the first solvation shell, and thus this feature should be a good measure of the homogeneous width of the ν_3 vibrational mode of FA in solid pH_2. To quantify the $n = 0$ feature line width, we fitted a sum of four Lorentzian lineshapes ($n = 0$ to 3) to the spectrum in trace b of Figure 6. The individual cluster lineshapes are also indicated in Figure 6 as thin lines. The data is well modeled by the sum of Lorentzian lineshapes and the full width at half-maximum (fwhm) of the $n = 0$ feature is 0.214(6) cm^{-1}. For comparison, the low pressure, room temperature gas-phase fwhm of individual rovibrational lines of the ν_3 mode of FA is 0.0045 cm^{-1}, where the width is due to a convolution of the Doppler width (0.0032 cm^{-1}) over the instrumental resolution (0.0036 cm^{-1}).[32] Previous studies of small nonrotating molecules (N_2O,

CH_3F, etc.) in solid pH_2 matrices have revealed absorption features with linewidths on the order of 0.01 cm^{-1}. We were therefore surprised that the fwhm of the ν_3 mode of FA in solid pH_2 is at least 50 times broader than the gas-phase value.

The cluster spectra in Figure 6 are better fit by a sum of Lorentzian lineshapes than Gaussian lineshapes (not shown) which implies the broadening mechanism is homogeneous. On the basis of the assumption of homogeneous broadening, the fwhm of the spectral transition is related to the population relaxation time (T_1) and the pure dephasing time (T'_2) as

$$\Gamma = \frac{1}{2\pi c T_1} + \frac{1}{\pi c T'_2} \tag{4}$$

where Γ is the fwhm of the Lorentzian line shape.[48,49] Previous studies have shown that at these low temperatures the contributions from pure dephasing to the dopant line width in solid pH_2 are negligible, and thus the observed line width directly reflects the population relaxation time.[48,49] Under this assumption, the vibrational relaxation time for the $v_3 = 1$ excited state of FA in solid pH_2 is 24.8 ps. Such a short $v_3 = 1$ excited-state lifetime seems unlikely given the sparseness of FA vibrational states at 1750 cm^{-1} excitation energies. Indeed, gas-phase measurements put a lower limit of $T_1 \geq 1.2$ ns on the vibrational relaxation time due to intramolecular vibrational energy redistribution (IVR). As demonstrated here for the ν_3 mode, the pH_2 matrix should not significantly perturb the anharmonic couplings in FA to cause such increased IVR rates, and there are no near-resonant pathways to dissipate the ~1750 cm^{-1} vibrational energy into the pH_2 solid. The ν_4, ν_5, and ν_6 modes are not too much lower in energy than the ν_3 mode and thus phonon or roton assisted cascade processes within the pH_2 solid can not be excluded. However, the more likely scenario is that this broadening still reflects some sort of inhomogeneous broadening mechanism. Recently, motivated by spectral measurements of molecules in helium nanodroplets, Lehmann pointed out that observation of a Lorentzian line shape alone is not sufficient proof to imply the width reflects population relaxation.[50]

Further clues to the origin of the residual broadening come from an examination of the $2\nu_3$ overtone data. As shown in Figure 5, the line width of the $n = 0$ feature is 0.45(2) cm^{-1} or more than two times broader than the $n = 0$ ν_3 fundamental peak. For comparison, the average $2\nu_3$ rovibrational line width for FA solvated in a helium nanodroplets is 0.03 cm^{-1}, more than 15 times narrower than the analogous measurements in solid pH_2.[28] This difference between superfluid helium and solid pH_2 would seem to suggest that inhomogeneous broadening in solid pH_2, not present in helium nanodroplets, is leading to increased linewidths. The origin of this inhomogeneous broadening could be interactions of FA with residual oH_2 far removed from the FA. The concentration of the oH_2 molecules that do not cluster with the FA remains constant on the approximate 6 h time scale of the experiment. The reason for this is the rate of o/p conversion in pure SMH is second-order with respect to the oH_2 concentration.[22] Thus, at the initial 45 ppm concentrations of the samples in these studies, the rate of o/p conversion is so slow that the bulk oH_2 concentration does not change appreciably.

If residual oH_2 in the crystal is responsible for the observed broadening of the $n = 0$ feature of FA, it is surprising that comparable linewidths were not observed for the ν_3 mode of CH_3F isolated in solid pH_2.[30] In both cases, large oH_2-induced shifts are observed, and thus distant oH_2 may contribute to broadening of the ν_3 transition. For CH_3F, upon complexation of a single oH_2, the ν_3 transition frequency shifts -0.71 cm^{-1} and for FA the shift is -0.32 cm^{-1}, yet the ν_3 line width for CH_3F is 12 times more narrow (0.018 cm^{-1}).[30] In addition, the matrix shift of the ν_3 vibration of FA (-8.20 cm^{-1}) and CH_3F (-8.42 cm^{-1}) are comparable. Since the matrix shift is proportional to the change in the dopant-pH_2 intermolecular interaction upon vibrational excitation, it again seems surprising that both vibrational modes have comparable matrix shifts but very different linewidths. One possibility is that since CH_3F is more compact and occupies a single substitution site within the crystal, while FA occupies a double or triple substitution site that the difference in linewidths reflects greater inhomogeneities in the solvation of FA in pH_2 caused by FA's greater perturbation of the local pH_2 crystal structure. Thus, we speculate that even though the $n = 0$ transition is well modeled by a Lorentzian line shape, which typically implies lifetime broadening, the breadth of the ν_3 transition reflects an inhomogeneous broadening mechanism other than oH_2 clustering.

5. Conclusions

The high-resolution (0.02 cm^{-1}) vibrational spectrum of FA isolated in solid pH_2 is presented. This investigation shows that all six of the FA normal mode absorptions studied show evidence of inhomogeneous broadening. In the case of the ν_3 carbonyl stretching mode, the dominant broadening mechanism is shown to be oH_2 clustering to FA. At low oH_2 concentrations, individual $FA(oH_2)_n$ cluster sizes are spectroscopically resolved in the ν_3 region for cluster sizes up to $n = 5$. The proof that oH_2 clustering is responsible for the multiple peak spectra is provided by electrostatic model calculations that agree well with the observed shifts in the ν_3 and $2\nu_3$ spectral regions and through time dependent observations of intracluster oH_2 to pH_2 nuclear spin conversion at low temperature.

The fact that individual absorption features for $FA(oH_2)_n$ clusters can be spectrally resolved in the ν_3 region emphasizes how oH_2 and pH_2 behave differently in SMH. Because of the symmetry restrictions placed on the rotational wave functions of these two nuclear spin states of molecular hydrogen, oH_2 in general has greater attractive intermolecular interactions with dopant molecules compared to pH_2 molecules such that oH_2 accumulates around the dopant during deposition and annealing. This preferential solvation of polar dopant species by trace oH_2 molecules present in highly enriched pH_2 solids is likely a general phenomenon; however identification and characterization of oH_2 clustering using IR spectroscopy of the dopant necessitates that replacing one pH_2 molecule by an oH_2 molecule in the first solvation shell of the dopant produces a resolvable frequency shift in the peak maxima of the dopant. Preferential clustering by oH_2 and cluster size dependent vibrational shifts have been measured for a variety of small molecules (CH_3F, N_2O, H_2O) of which now FA can be added to the list. These spectroscopic results also indicate that matrix isolation studies carried out in nH_2 and enriched pH_2 matrices will typically produce slightly different dopant vibrational frequencies due to the greater vibrational shifts caused by the oH_2 species.

Acknowledgment. The authors wish to acknowledge the contributions of Sharon C. Kettwich, Dr. Paul L. Raston, and Dr. Robert C. Corcoran. Further, we gratefully acknowledge Dr. Jan Kubelka for his assistance in calculating the ground- and excited-state dipole moments of formic acid. This work was sponsored by the Chemistry Division of the US National Science Foundation (CHE 03-16268).

References and Notes

(1) Oka, T. *Annu. Rev. Phys. Chem.* **1993**, *44*, 299.

(2) Weliky, D. P.; Kerr, K. E.; Byers, T. J.; Zhang, Y.; Momose, T.; Oka, T. *J. Chem. Phys.* **1996**, *105*, 4461.

(3) Momose, T.; Miki, M.; Wakabayashi, T.; Shida, T.; Chan, M.-C.; Lee, S. S.; Oka, T. *J. Chem. Phys.* **1997**, *107*, 7707.

(4) Sogoshi, N.; Wakabayashi, T.; Momose, T.; Shida, T. *J. Phys. Chem. A* **1997**, *101*, 522.

(5) Mengel, M.; Winnewisser, B. P.; Winnewisser, M. *J. Low Temp. Phys.* **1998**, *111*, 757.

(6) Tam, S.; Fajardo, M. E.; Katsuki, H.; Hoshina, H.; Wakabayashi, T.; Momose, T. *J. Chem. Phys.* **1999**, *111*, 4191.

(7) Hinde, R. J.; Anderson, D. T.; Tam, S.; Fajardo, M. E. *Chem. Phys. Lett.* **2002**, *356*, 355.

(8) Kuroda, K.; Koreeda, A.; Takayangi, S.; Suzuki, M.; Hakuta, K. *Phys. Rev. B* **2003**, *67*, 184303.

(9) Lindsay, C. M.; Oka, T.; Momose, T. *J. Mol. Spectrosc.* **2003**, *218*, 131.

(10) Hinde, R. J. *J. Chem. Phys.* **2003**, *119*, 6.

(11) Fajardo, M. E.; Tam, S.; DeRose, M. E. *J. Mol. Struct.* **2004**, *695–696*, 111.

(12) Andrews, L. *Chem. Soc. Rev.* **2004**, *33*, 123.

(13) Momose, T.; Oka, T. *J. Low Temp. Phys.* **2005**, *139*, 515.

(14) Ceponkus, J.; Nelander, B. *J. Chem. Phys.* **2006**, *124*, 024504.

(15) Mishra, A. P.; Balasubramanian, T. K. *J. Chem. Phys.* **2006**, *125*, 124507.

(16) Wang, X.; Andrews, L. *Angew. Chem., Int. Ed.* **2007**, *46*, 2602.

(17) Lee, Y. C.; Venkatesan, V.; Lee, Y. P.; Macko, P.; Didiriche, K.; Herman, M. *Chem. Phys. Lett.* **2007**, *435*, 247.

(18) Fajardo, M. E.; Lindsay, C. M. *J. Chem. Phys.* **2008**, *128*, 014505.

(19) Lee, Y. P.; Wu, Y. J.; Hougen, J. T. *J. Chem. Phys.* **2008**, *129*, 104502.

(20) Abouaf-Marguin, L.; Vasserot, A.-M.; Pardanaud, C.; Stienlet, J.; Michaut, X. *Chem. Phys. Lett.* **2008**, *454*, 61.

(21) Kettwich, S. C.; Pinelo, L. F.; Anderson, D. T. *Phys. Chem. Chem. Phys.* **2008**, *10*, 5564.

(22) Silvera, I. F. *Rev. Mod. Phys.* **1980**, *52*, 393.

(23) Van Kranendonk, J. *SOLID HYDROGEN: Theory of the Properties of Solid H_2, HD, and D_2*; Plenum Press: New York, 1983.

(24) Redington, R. L. *J. Mol. Spectrosc.* **1977**, *65*, 171.

(25) Lundell, J.; Rasanen, M.; Latajka, Z. *Chem. Phys.* **1994**, *189*, 245.

(26) Macoas, E. M. S.; Lundell, J.; Pettersson, M.; Khriachtchev, L.; Fausto, R.; Rasanen, M. *J. Mol. Spectrosc.* **2003**, *219*, 70.

(27) Marushkevich, K.; Khriachtchev, L.; Rasanen, M. *Phys. Chem. Chem. Phys.* **2007**, *9*, 5748.

(28) Madeja, F.; Markwick, P.; Havenith, M.; Nauta, K.; Miller, R. E. *J. Chem. Phys.* **2002**, *116*, 2870.

(29) Pettersson, M.; Lundell, J.; Khriachtchev, L.; Rasanen, M. *J. Am. Chem. Soc.* **1997**, *119*, 11715.

(30) Yoshioka, K.; Anderson, D. T. *J. Chem. Phys.* **2003**, *119*, 4731.

(31) Buckingham, A. D. *Adv. Chem. Phys.* **1967**, *12*, 107.

(32) Weber, W. H.; Maker, P. D.; Johns, J. W. C.; Weinberger, E. *J. Mol. Spectrosc.* **1987**, *121*, 243.

(33) Frisch, M. J.; Trucks, G. W.; Schlegel, H. B.; Scuseria, G. E.; Robb, M. A.; Cheeseman, J. R.; Montgomery, J. A., Jr.; Vreven, T.; Kudin, K. N.; Burant, J. C.; Millam, J. M.; Iyengar, S. S.; Tomasi, J.; Barone, V.; Mennucci, B.; Cossi, M.; Scalmani, G.; Rega, N.; Petersson, G. A.; Nakatsuji, H.; Hada, M.; Ehara, M.; Toyota, K.; Fukuda, R.; Hasegawa, J.; Ishida, M.; Nakajima, T.; Honda, Y.; Kitao, O.; Nakai, H.; Klene, M.; Li, X.; Knox, J. E.; Hratchian, H. P.; Cross, J. B.; Bakken, V.; Adamo, C.; Jaramillo, J.; Gomperts, R.; Stratmann, R. E.; Yazyev, O.; Austin, A. J.; Cammi, R.; Pomelli, C.; Ochterski, J. W.; Ayala, P. Y.; Morokuma, K.; Voth, G. A.; Salvador, P.; Dannenberg, J. J.; Zakrzewski, V. G.; Dapprich, S.; Daniels, A. D.; Strain, M. C.; Farkas, O.; Malick, D. K.; Rabuck, A. D.; Raghavachari, K.; Foresman, J. B.; Ortiz, J. V.; Cui, Q.; Baboul, A. G.; Clifford, S.; Cioslowski, J.; Stefanov, B. B.; Liu, G.; Liashenko, A.; Piskorz, P.; Komaromi, I.; Martin, R. L.; Fox, D. J.; Keith, T.; Al-Laham, M. A.; Peng, C. Y.; Nanayakkara, A.; Challacombe, M.; Gill, P. M. W.; Johnson, B.; Chen, W.; Wong, M. W.; Gonzalez, C.; Pople, J. A. *Gaussian 03*, revision C.02; Gaussian, Inc.: Wallingford, CT, 2004.

(34) Takahashi, K.; Sugawara, M.; Yabushita, S. *J. Phys. Chem. A* **2002**, *106*, 2676.

(35) Freytes, M.; Hurtmans, D.; Kassi, S.; Lievin, J.; Vander Auwera, J.; Campargue, A.; Herman, M. *Chem. Phys.* **2002**, *283*, 47.

(36) Fajardo, M. E.; Tam, S. *J. Chem. Phys.* **1998**, *108*, 4237.

(37) Tam, S.; Fajardo, M. E. *Rev. Sci. Instrum.* **1999**, *70*, 1926.

(38) Yoshioka, K.; Anderson, D. T. *J. Mol. Struct.* **2006**, *786*, 123.

(39) Anderson, D. T.; Hinde, R. J.; Tam, S.; Fajardo, M. E. *J. Chem. Phys.* **2002**, *116*, 594.

(40) Tam, S.; Fajardo, M. E. *Appl. Spectrosc.* **2001**, *55*, 1634.

(41) Tam, S.; Fajardo, M. E. *Low Temp. Phys.* **2000**, *26*, 653.

(42) Lorenz, B. D.; Anderson, D. T. *J. Chem. Phys.* **2007**, *126*, 184506.

(43) Jacox, M. E. *J. Mol. Spectrosc.* **1985**, *113*, 286.

(44) Jacox, M. E. *Chem. Phys.* **1994**, *189*, 149.

(45) Lide, D. R. *CRC Handbook of Chemistry and Physics*, 82nd ed.; CRC Press LLC: Boca Raton, FL, 2001.

(46) Momose, T.; Fushitani, M.; Hoshina, H. *Int. Rev. Phys. Chem.* **2005**, *24*, 533.

(47) Hallam, H. E. *Vibrational spectroscopy of trapped species; infrared and Raman studies of matrix-isolated molecules, radicals and ions*; John Wiley & Sons: New York, 1973.

(48) Katsuki, H.; Momose, T. *Phys. Rev. Lett.* **2000**, *84*, 3286.

(49) Fajardo, M. E.; Lindsay, C. M. *J. Chem. Phys.* **2008**, *128*, 014505.

(50) Lehmann, K. K. *J. Chem. Phys.* **2007**, *126*, 024108.

JP8100255